

RESEARCH ARTICLE

Interstitial ultrasound ablation of vertebral and paraspinal tumours: Parametric and patient-specific simulations

Serena J. Scott^{1,2}, Vasant Salgaonkar¹, Punit Prakash³, E. Clif Burdette⁴, & Chris J. Diederich^{1,2}

¹Thermal Therapy Research Group, Department of Radiation Oncology, University of California, San Francisco, California, ²University of California, Berkeley – University of California, San Francisco Graduate Program in Bioengineering, California, ³Department of Electrical and Computer Engineering, Kansas State University, Manhattan, Kansas, and ⁴Acoustic MedSystems, Savoy, Illinois, USA

Abstract

Purpose: Theoretical parametric and patient-specific models are applied to assess the feasibility of interstitial ultrasound ablation of tumours in and near the spine and to identify potential treatment delivery strategies.

Methods: 3D patient-specific finite element models ($n = 11$) of interstitial ultrasound ablation of tumours associated with the spine were generated. Gaseous nerve insulation and various applicator configurations, frequencies (3 and 7 MHz), placement trajectories, and tumour locations were simulated. Parametric studies with multilayered models investigated the impacts of tumour attenuation, tumour dimension, and the thickness of bone insulating critical structures. Temperature and thermal dose were calculated to define ablation (>240 equivalent minutes at 43 °C (EM43 °C)) and safety margins (<45 °C and <6 EM43 °C), and to determine performance and required delivery parameters.

Results: Osteolytic tumours (≤ 44 mm) encapsulated by bone could be successfully ablated with 7 MHz interstitial ultrasound (8.1–16.6 W/cm², 120–5900 J, 0.4–15 min). Ablation of tumours (94.6–100% volumetric) 0–14.5 mm from the spinal canal was achieved within 3–15 min without damaging critical nerves. 3 MHz devices provided faster ablation (390 versus 930 s) of an 18 mm diameter osteoblastic (high bone content) volume than 7 MHz devices. Critical anatomy in proximity to the tumour could be protected by selection of appropriate applicator configurations, active sectors, and applied power schemas, and through gaseous insulation. Preferential ultrasound absorption at bone surfaces facilitated faster, more effective ablations in osteolytic tumours and provided isolation of ablative energies and temperatures.

Conclusions: Parametric and patient-specific studies demonstrated the feasibility and potential advantages of interstitial ultrasound ablation treatment of paraspinal and osteolytic vertebral tumours.

Keywords

Bone, interstitial ultrasound, theoretical model, thermal ablation

History

Received 24 December 2013

Revised 13 March 2014

Accepted 14 April 2014

Published online 10 July 2014

Introduction

The skeleton is a common site of cancer metastasis, with an incidence of 65–75% observed upon autopsy among breast and prostate cancer patients [1]. The spine is the most common location of bone metastases, with tumours observed in up to 40% of cancer patients during autopsy [2]. Primary bone tumours are far less common, making up only 0.2% of primary neoplasms [3]. Soft tissue tumours in the paraspinal spaces are also rare [4]. While survival rates for some forms of primary bone cancer are relatively high (60% for localised osteosarcoma and Ewing's sarcoma) [5,6], the prognosis for patients with bone metastases is often very poor, so treatment

goals for metastatic bone disease are generally palliative [7,8]. The principle aims of palliative care for bone metastases are pain relief and restoration or preservation of both mechanical and neurological function [7]. Treatment options for primary and metastatic bone tumours include radiation, surgery, drugs, and thermal ablation [9–11]. Surgery and radiation, particularly intensity-modulated radiotherapy, are two means of treating paraspinal tumours [4,12,13]. External beam radiation is the standard of care for treatment of painful bone metastases [8,9,14], while radiofrequency (RF) ablation is now the standard of care for treatment of osteoid osteoma of the appendicular skeleton [14,15]. To mechanically stabilise eroded or fractured bones and to provide further pain relief, radiotherapy and thermal ablation can both be performed in conjunction with cement injection into cavities in bone [7,16,17].

Minimally invasive thermal ablation using radiofrequency (RF) currents [10,16,18–20], plasma-mediated RF [21,22], lasers [23], microwaves [24], and cryoablation [25] has been applied to successfully treat neoplasms throughout the

Correspondence: Chris J. Diederich, PhD, Thermal Therapy Research Group, University of California, San Francisco, 1600 Divisadero Street, Suite H1031, San Francisco, CA 94143-1708, USA. Tel: (415) 476-8641. Fax: (415) 353-9883. E-mail: cdiederich@radonc.ucsf.edu

skeleton [9,22], with RF ablation the most common. Image-guided high intensity focused ultrasound (HIFU) ablation of bone tumours has also gained attention in recent years for palliative treatment of painful metastases, most likely through ablation of the pain-sensing nerves in the periosteum at bone surfaces, with tumours of the spine contraindicated [26–28]. The volumes treated with thermal ablation vary widely in size, from 5 mm osteoid osteomas to 10 cm regions of coagulation in chordomas [23,29]. During ablation, the spinal cord and spinal nerves should be kept below 45 °C [18] and 10–30 EM43 °C [30] to prevent neurological damage; thus, tumours in very close proximity (within 1 cm) to the spinal cord have sometimes been considered an exclusion criteria for RF ablation [19]. Cortical and cancellous bone surrounding vertebral tumours, due to inherent low thermal conductivities, can thermally insulate the spinal cord, allowing for ablation of some vertebral lesions that do not invade the spinal canal [18]. However, despite the lack of insulating bone, vertebral tumours immediately adjacent to the spinal canal have been successfully treated with thermal ablation [16,18]. The lack of neurological complications following these procedures has been attributed to the cooling flows of cerebrospinal fluid (CSF) and of blood within epidural vessels [20], as well as to the feedback of patients under conscious sedation [16]. In some cases with posterior wall destruction, gaseous dissection applied to displace and insulate the spinal cord successfully prevented neurological complications during laser ablation, RF ablation, and cryoablation [23,31].

Compared to other minimally invasive percutaneous approaches, interstitial ultrasound has potential advantages which can be exploited for ablation of paraspinal tumours and osteolytic tumours within the spine. Interstitial ultrasound ablation has been successfully applied in this setting in preliminary studies using numerical simulations and in vivo rabbit models [32,33]. Interstitial ultrasound applicators can be designed with multiple angularly sectorised cylindrical transducers, providing penetrating directional control along the length and circumference of the applicator [34]. Furthermore, the high acoustic absorption coefficient of bone, one to two orders of magnitude above that of soft tissue [35], limits energy penetration and produces significant heating at the bone surfaces [36]. Thus, bone adjacent to or encapsulating a tumour may isolate the acoustic energy and effectively produce a secondary heat source away from the ultrasound applicator, enhancing heating [37,38]. Bone adjacent to a tumour can also serve to protect nearby sensitive structures, such as the spinal cord, through acoustic and thermal insulation [18]. Interstitial ultrasound devices are compatible with MR temperature imaging (MRTI), which could be applied as a means to monitor treatment in real time and to provide feedback control of power [39].

The goal of this paper is develop and apply acoustic and biothermal finite element models to characterise the performance of and assess the feasibility of interstitial ultrasound ablation of tumours in and near the spine. The focus is not patient-specific treatment planning. Parametric studies with simplified models were performed to determine the influence of acoustic attenuation, blood perfusion, gaseous insulation of nerve tissue, preferential bone heating, and the thickness of encapsulating bone on the resulting temperatures and thermal

dose distributions, as well as on the required power levels and treatment durations. To assess treatment delivery strategies, 11 3D patient-specific models of interstitial ultrasound ablation of nine vertebral and paraspinal tumours were developed, simulating treatments with a variety of applicator configurations, operating frequencies, and insertion paths. In order to determine how disparate material properties among tissues and vascular cooling affect heating distributions, several anatomical structures, including the tumour, bones, spinal canal, intervertebral discs, lungs, and major blood vessels, were considered. The findings of this study evaluate applicator configurations, insertion strategies, and treatment parameters (power, frequency, time) for tumours in the vicinity of the spine of various sizes, shapes, and locations.

Materials and methods

Interstitial ultrasound applicators

The interstitial ultrasound applicators considered in this study are described in detail elsewhere [34,40] and are modelled herein as a linear array of 1–4 tubular ultrasound transducers with 150–360° angular sectors. Transducer arrays operating at a nominal frequency of 7 MHz, a typical interstitial ultrasound configuration [34,41], and 3 MHz were considered. The 7 MHz transducers (5, 10, or 15 mm length (L), 1.5 mm overall diameter (OD)) were operated inside a 1.89 mm inner diameter (ID), 2.4 mm OD plastic catheter; 3 MHz transducers (5 or 15 mm L, 3.2 mm OD) were considered for greater penetration into tumours with high ultrasound attenuation coefficients, and were operated from within a 4 mm ID, 4.5 mm OD plastic catheter. Integrated water cooling of the inner catheter surface was employed for each applicator configuration. Based upon prior experimental measurements, it was assumed in this work that 50% of the applied electrical power was converted to acoustic output power [34,42].

Biothermal and acoustic simulations

Two sets of models were developed: simple geometric models for parametric studies, and patient-specific models including complex osseous and soft tissue structures for more detailed assessments. Pennes' bioheat transfer equation was used to model heat transfer in heterogeneous tissues [43]:

$$\rho c \frac{dT}{dt} = \nabla \cdot k \nabla T - \omega c_b (T - T_b) + Q \quad (1)$$

where ρ is density (kg/m³), c is specific heat capacity (J/kg/°C), T is temperature (°C), t is time (s), k is thermal conductivity (W/m/°C), ω is blood perfusion (kg/m³/s), Q is heat deposition due to ultrasound (W/m³), the subscript b refers to blood, and $T_b = 37$ °C. The various tissue properties are summarised in Table I. Tumour composition is assumed to be homogenous throughout the tumour volume. Thermal dose (t_{43}) in equivalent minutes at 43 °C (EM43 °C) is calculated according to Sapareto and Dewey [44], with tissue considered to be ablated upon reaching a thermal dose of 240 EM43 °C [45].

$$t_{43} = \sum_{t=0}^{t=final} R^{43-T} \Delta t, \quad R = \begin{cases} 0.5, & T > 43 \\ 0.25, & T \leq 43 \end{cases} \quad (2)$$

Table I. Material properties of tissues.

Medium	Density (kg/m ³)	Velocity (m/s)	Attenuation (Np/m/MHz)	Thermal conductivity (W/m/°C)	Specific heat (J/kg/°C)	Perfusion rate (kg/m ³ /s)
Muscle	1041 [35]	1576 [35]	5 [75]	0.5 [35]	3430 [35]	0.6923 [35]
Bone	1420 [35]	3260 [35]	105 [35]	0.38 [35]	1700 [35]	0.892 [76]
Spinal canal and nerves	1038 [35]	1542 [35]	12 [†] [35]	0.515 [†] [35]	3640 [‡] [35]	3.63 [77]
Intervertebral disc	1165* [35]	1627** [78]	53.3* [35]	0.61 [79]	2713 [79]	0 [80]
Carbon dioxide	1.66 [81]			0.018 [81]	871.5 [81]	0
Blood					3800 [35]	

Tumour tissue is assumed to have the same properties as muscle, but with a higher perfusion of 2.4 kg/m³/s [82,83]. Values for nerve ([†]) and brain ([‡]) were used for some spinal canal properties. Values for tendon (*) and cartilage (**) were used for some intervertebral disc properties.

Perfusion in all tissues is assumed to reduce to zero at 300 EM43 °C due to heating-induced microvascular stasis [46].

Acoustic heat deposition from a cylindrical interstitial ultrasound source can be modelled as a radially divergent intensity pattern well collimated to the length of the transducer [41]. This model was experimentally validated by our group in bone/soft tissue phantoms and in ex vivo bones and soft tissues, through comparison to temperature distributions derived both invasively and using MRTI [38,47,48].

$$Q = 2\alpha I = 2\tau\alpha I_s \frac{r_t}{r} e^{-2\int_n^r \mu dr'} \quad (3)$$

where α is the ultrasound absorption coefficient (Np/m), I is acoustic intensity (W/m²), τ is the transmission coefficient (unitless), I_s is the acoustic intensity on the transducer surface (W/m²), r_t is the transducer radius (m), r is the radial distance from the transducer's central axis (m), and μ is the ultrasound attenuation coefficient (Np/m). The ultrasound absorption coefficient is assumed to be equal to the ultrasound attenuation coefficient, with all scattered energy locally absorbed. Attenuation over the catheter wall is assumed to be 43.9 Np/m/MHz [49]. The power applied to a transducer sector was either constant over time or determined by a proportional-integral (PI) feedback controller ($k_p = 0.375$ W/K, $k_i = 0.003$ W/K/s) designed to maintain the maximum temperature in a region of interest (ROI) at a given value T_c . The acoustic intensity on the transducer surface (I_s) was limited to a practical and achievable value of 21.2 W/m².

The absorption of incident waves by soft tissue and bone contributes significantly more to heat generation than do reflected waves at most incident angles encountered during interstitial ultrasound ablation [37,38]. High-frequency (~7 MHz) ultrasound waves in bone are attenuated so rapidly that they do not penetrate deep enough for refraction or shear mode conversion to significantly affect temperature distributions [38]. Hence, following the findings of Scott et al., the transmission coefficient into a given tissue can be approximated as [38]:

$$\tau \equiv \prod_{i=2}^n \frac{I_i}{I_{i-1}} = \prod_{i=2}^n \frac{4\rho_i \nu_i \rho_{i-1} \nu_{i-1}}{(\rho_i \nu_i + \rho_{i-1} \nu_{i-1})^2} \quad (4)$$

where ν is the speed of sound (m/s) and the structures that are traversed are numbered 1 through n , beginning with the catheter. It is assumed that there is zero transmission through tissue/gas boundaries, and that the catheter has the same acoustic properties as osteolytic tumours for

Table II. Heat transfer coefficients and fluid temperatures for convective flow boundaries.

Surface	h (W/m ² /°C)	T_f (°C)
Catheter	1000 [47,84]	22
Aorta	598	37
Vena cava	391	37
Carotid artery and jugular vein	970	37
Lungs and respiratory passages	40 [85]	34 [86]
Skin	10.5 [85,87]	22

Heat transfer coefficients for blood vessels are calculated based upon vessel diameters and flow rates [88–90] as described by Haemmerich et al. [91].

complete acoustic transmission into the catheter and osteolytic tumours.

Finite element analysis

Finite element analysis was performed using COMSOL Multiphysics 4.3 (Burlington, MA) in conjunction with MATLAB (MathWorks, Natick, MA) to calculate acoustic intensity, power deposition, temperature, and thermal dose. Simulations employing various mesh sizes and time steps were performed to determine how small the mesh sizes and time steps should be in order for the results to converge to a stable solution. Based upon these tests, maximum mesh sizes were limited to 0.4 mm on the inner surfaces of the catheter, 0.5 mm on heated bone surfaces, and 5 mm overall, with gradual transitions in mesh size. An implicit transient solver with variable time stepping was used to calculate temperature and thermal dose, with maximum time steps of 10 s. Dirichlet boundary conditions constrained the temperature on the outermost tissue boundaries to 37 °C. Convective boundary conditions were applied to inner catheter surfaces, major blood vessels, respiratory passages, and skin surfaces as follows:

$$-\hat{n} \cdot (-k\nabla T) = h(T_f - T) \quad (5)$$

where \hat{n} is the normal unit vector to the boundary, h is the heat transfer coefficient (W/m²/°C), and T_f (°C) is the fluid temperature, with parameters specified in Table II.

Parametric studies

Parametric studies were performed using simplified 3D models to determine the influence of tumour attenuation (which is related to osseous bone content), preferential

heating of encapsulating bone, tumour perfusion, gaseous insulation, and the thickness of encapsulating bone on resulting temperature distributions, on thermal dosimetry, and on required treatment delivery parameters. The simple geometry consisted of a 7.2 cm long cylindrical tumour volume with a 7 MHz applicator positioned within the centre. Depending upon the complexity of the parametric study, the geometry could include an annular layer of bone, a layer of carbon dioxide, and a surrounding layer of non-targeted tissue (Figure 1). In all cases the applicator was modelled with three $360^{\circ} \times 1$ cm long transducers operating at 7 MHz, and the total outer diameter was 11 cm. Finite element meshes representing these volumes were generated within COMSOL. These parametric studies were performed in 2D axisymmetric mode, as the tubular ultrasound transducers and cylindrical tissue volumes considered could be accurately represented as rectangles revolved around an axis, and because computation times were many times faster than those of the equivalent 3D models. A PI controller modulated the power delivered to the transducers to attain a

peak temperature T_c within a ROI. The maximum control temperature set-point (T_c) was 75° , 80° , or 85°C , for temperatures high enough to ablate the full tumour but low enough to prevent water vaporisation in tissue. The ROI was defined as a 1 cm high portion of the tumour around the central transducer, ranging radially from 1 mm away from the outer surface of the catheter to the bone surface. The thermal lesion diameter was defined as the maximum diameter of the $240\text{ EM43 }^{\circ}\text{C}$ contour, and an ROI was considered ablated when its entire volume reached $240\text{ EM43 }^{\circ}\text{C}$ [45]. The geometric and treatment parameters of the parametric studies performed are summarised in Table III and are detailed below.

Effect of attenuation on thermal lesion size

For investigations of the effect of tumour attenuation on thermal lesion size, a tumour was modelled with ultrasound attenuation coefficients varying from 3 to 300 Np/m/MHz , a range encompassing the low attenuations of some soft tissues, the moderate to high attenuations expected in tumours with residual pieces of osseous bone, and the high attenuations observed in some bones [35]. Encapsulating bone was not considered.

Effect of bone on treatment parameters

To determine how bone adjacent to or encapsulating an unossified tumour affects the treatment parameters necessary to ablate an ROI, a parametric study was performed, simulating highly osteolytic tumours of various diameters encapsulated within bone. An applicator was placed in the centre of a tumour surrounded by bone. The power levels and treatment durations necessary to ablate the ROI, as well as the maximum bone temperature at the end of the ablation, were determined for various tumour diameters ($0.6\text{--}5\text{ cm}$) and perfusions ($0.7\text{--}5\text{ kg/m}^3/\text{s}$).

Thermal dose on spinal cord insulated by bone

Given the spinal cord and nerves in close proximity to targets within the vertebrae, we investigated the insulating effects of normal bone and of gaseous dissection to determine the treatment parameters and criteria necessary to protect sensitive tissue. As shown in Figure 1, an applicator was modelled in the centre of a tumour ($6\text{--}40\text{ mm OD}$), surrounded by bone ($2\text{--}4\text{ mm thick}$), surrounded by an annular layer of ‘sensitive’ nerve tissue (11 cm OD). The maximum thermal dose on the spinal canal was calculated for control temperatures T_c of 75° , 80° , and 85°C . To determine the effects of additional gaseous insulation, the geometry of Figure 1 was modified to consider

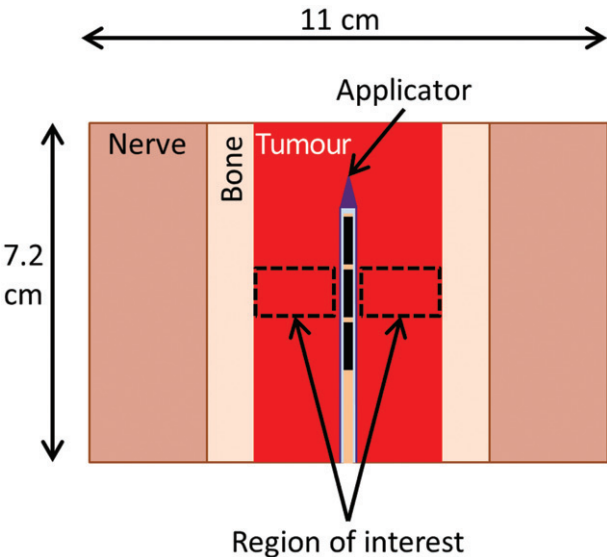


Figure 1. The geometry of the parametric simulations consisted of a 7.2 cm L, 11 cm OD cylinder with an applicator in the centre. The applicator consists of a series of transducers (black) mounted operated within a water-cooled catheter (purple). The tissues ablated could consist of only tumour tissue, tumour surrounded by bone, or tumour surrounded by bone surrounded by nerve tissue. There could also be a layer of carbon dioxide between the bone and nerve tissue. The temperature of a 1 cm long region of interest in the centre of the tumour was controlled to a maximum temperature T_c .

Table III. Treatment and geometric parameters for parametric studies.

Parametric study	Effect of attenuation on thermal lesion size	Effect of bone on treatment parameters	Thermal dose on spinal cord insulated by bone
Tumour diameter	11 cm OD	0.6–5.6 cm OD	0.6–4.0 cm OD
Bone dimensions	N/A	11 cm OD	2, 3, 4 mm thick
Insulating gas thickness	N/A	N/A	0, 2 mm
Nerve diameter	N/A	N/A	11 cm OD
Tumour attenuation	3–300 Np/m/MHz	5 Np/m/MHz	5 Np/m/MHz
Control temperature	75° , 85°C	75° , 85°C	75° , 80° , 85°C
Tumour perfusion	$2.4\text{ kg/m}^3/\text{s}$	0.7, 2.4, $5\text{ kg/m}^3/\text{s}$	$2.4\text{ kg/m}^3/\text{s}$
Treatment duration	5, 10, 15 min	Until ROI ablated	Until ROI ablated

cases with and without a 2 mm layer of carbon dioxide between the nerves and a 2 mm thickness of bone, with control temperatures of 85 °C.

Patient-specific models

To critically assess the feasibility and performance of interstitial ultrasound ablation in a variety of tumours within and near the spine, and to investigate treatment delivery strategies, 11 patient-specific models with a variety of tumour locations and dimensions were generated. Unlike the parametric studies in the previous section, this patient-specific study is based upon full 3D thermal and acoustic models which comprehensively consider the heterogeneous tissue properties of the irregularly shaped anatomical structures. Tumours (Table IV) were either segmented directly from 3D computed tomography (CT) image sets, or were based on the

shapes, sizes, and positions of tumours observed in patient data or in the literature [50–54]. Image segmentation and the generation of patient-specific finite element method (FEM) meshes (Figure 2) were performed using the Mimics Innovation Suite (Materialise, Leuven, Belgium), with tumours, vertebrae and other bones, intervertebral discs, the spinal canal, other soft tissues, major blood vessels, and airways differentiated. While many of the built-in automated segmentation tools were employed, the majority of the segmentation was performed manually. The FEM meshes were imported into COMSOL, in which the tissue and cooling flow properties specified in Tables I and II were applied and finite element analysis was performed. Applicator configurations and applied power levels were empirically determined for each case, based on the size of the tumour, the distance from the transducers to the bone surfaces, and the distance from the tumour to sensitive anatomy. Powers were either

Table IV. Location, bone content, and size of tumours considered in patient-specific models.

Case	Tumour location	Tumour type	Tumour dimensions (mm)	Tumour volume (mm ³)	Distance from tumour to critical structures (mm)
1	Between C4 and C5	Paraspinal	20 L, 19 OD 20 × 17 × 16	3200	SC: 6.8
2	T5, left transverse process	Osteolytic	20 L, 22 OD 20 × 20 × 19	4400	SC: 14, Lu: 6.0, Ao: 32
3	L3, left transverse process	Osteolytic	33 L, 27 OD 29 × 28 × 20	8100	SC: 4.5
4a–b	L2, pedicle, vertebral body, spinal canal	Osteolytic	43 L, 27 OD 43 × 27 × 27	9200	SC: 0, Ao: 28, VC: 22
5	C5, vertebral body	Osteolytic	10 L, 10 OD 10 × 10 × 10	520	SC: 2.6, F: 4.5, Tr: 15, Oe: 15, C: 18
6	L1, vertebral body	Osteolytic	25 L, 13 OD 25 × 13 × 13	2040	SC: 4.3, Ao: 13
7	L1, anterior vertebral body	Osteolytic	23 L, 27 OD 25 × 27 × 18	6600	SC: 13, Ao: 10, VC: 26
8	S1	Osteolytic	24 L, 17 OD 24 × 17 × 15	3200	SC and N: 2.9
9a–b	Iliac bone	A: Osteolytic B: Mixed	32 L, 18 OD 32 × 18 × 15	4900	SC and N: 12

SC, Spinal canal; Lu, Lung; Ao, Aorta; VC, Vena cava; F, Transverse foramen; Tr, Trachea; OD, overall diameter; Oe, Oesophagus; C, Carotid artery and internal jugular vein, N, Spinal nerves. Tumour length and diameter are defined in relation to the applicator axis. Next, the dimensions of a rectangular prism around the tumour are listed.

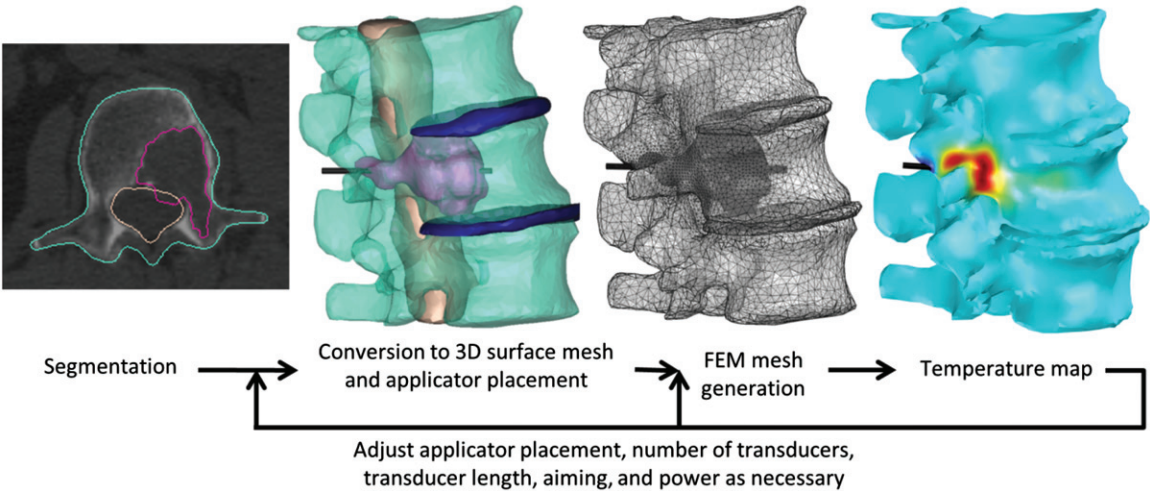


Figure 2. Process by which patient-specific simulations are created. 3D anatomy in a CT scan is segmented and converted into 3D surface meshes. The surface meshes of the anatomy and of a cylinder representing the applicator are combined and then converted into a finite element method (FEM) mesh, on which temperature and thermal dose are calculated.

constant throughout treatment or were determined by a PI controller designed to attain a maximum temperature T_c of 85 °C in an ROI defined as the tumour and adjacent bones. Practical applicator configurations with one to four transducers (0.5, 1, or 1.5 cm L) and 360° sectors, two sectors of 150° and 210°, or two 180° sectors were considered. On either side of each active transducer sector, a 15° acoustically inactive dead zone is assumed, as verified in previous experimental studies [55]. At the end of each ablation sequence, power and catheter cooling were shut off simultaneously, and thermal conduction through the tissues and cumulative thermal dose were modelled over an additional 10 min.

To investigate the effect of injected carbon dioxide as a possible means of insulating the spinal canal, interstitial ultrasound ablation of a vertebral tumour invading the pedicle and the spinal canal was modelled with and without carbon dioxide dissection in cases 4a and 4b, respectively (Table IV). A 2.6 cm³ CO₂ gas bubble was added in the spinal canal between the spinal cord and the tumour target in the 3D surface meshes of the anatomy and in the FEM mesh. Carbon dioxide was modelled with the material properties specified in Table I and with a gas/tissue acoustic transmission coefficient of zero. Separate feedback controllers determined the powers applied to each transducer. Power to each transducer element was permanently shut off 5 s after the tumour tissue around it was fully ablated (>240 EM43 °C), 5 s after the portion of the spinal canal next to it reached a thermal dose limit of 2 EM43 °C (to prevent nervous injury), or after 15 min of treatment, whichever occurred first. To ensure ablation of tissue adjacent to the water-cooled catheter via conduction, whenever power to a transducer was shut off, cooling flow and power to all other transducers were temporarily shut off for 10 s.

Patient-specific simulations (Table IV) of treatment targeting a 4.9 cm² tumour in the iliac bone (case 9) were performed to investigate whether a low frequency applicator

(3 MHz) could provide greater penetration than a 7 MHz applicator into a mixed osteolytic/osteoblastic lesion, which has higher bone content and a correspondingly higher acoustic attenuation coefficient than highly osteolytic lesions. The tumour was assumed to have the same attenuation as bone, with all other tumour properties assumed to be the same as those of osteolytic tumours (Table I). Identical applicator positions and feedback control parameters were used for both applicator test configurations. For these specific test evaluations, power and cooling flow were shut off 100 s after the entire tumour had reached 1000 EM43 °C, to ensure full ablation of the both the tumour and a margin of normal iliac bone.

Results

Parametric studies

Interstitial ultrasound ablation of tumours with a range of ultrasound attenuation coefficients was simulated. The diameters of the thermal lesions produced were measured for 5, 10, and 15 min treatment times and for control temperatures of 75° and 85 °C (Figure 3). Larger diameters (up to 52–59 mm) could be ablated in cases when the tumour had lower attenuations, when longer treatment times were used, and/or when higher control temperatures were used. At very high attenuations above ~80 Np/m/MHz, there was very little acoustic penetration, temperatures peaked within 1.5 mm of the catheter surface, and the maximum diameter that could be ablated varied relatively little with further increases in attenuation. Thus, in tumours with attenuations ranging from 3 to 100 Np/m/MHz, the lesion diameters created in 10 min with a control temperature of 85 °C varied 29.1 mm, while the thermal lesion diameters in tumours with attenuations of 200 to 300 Np/m/MHz only varied 0.9 mm.

Ablation of soft tissue lesions encapsulated within bone (Figure 1) was simulated for a variety of lesion diameters to determine the necessary powers and ablation times and the

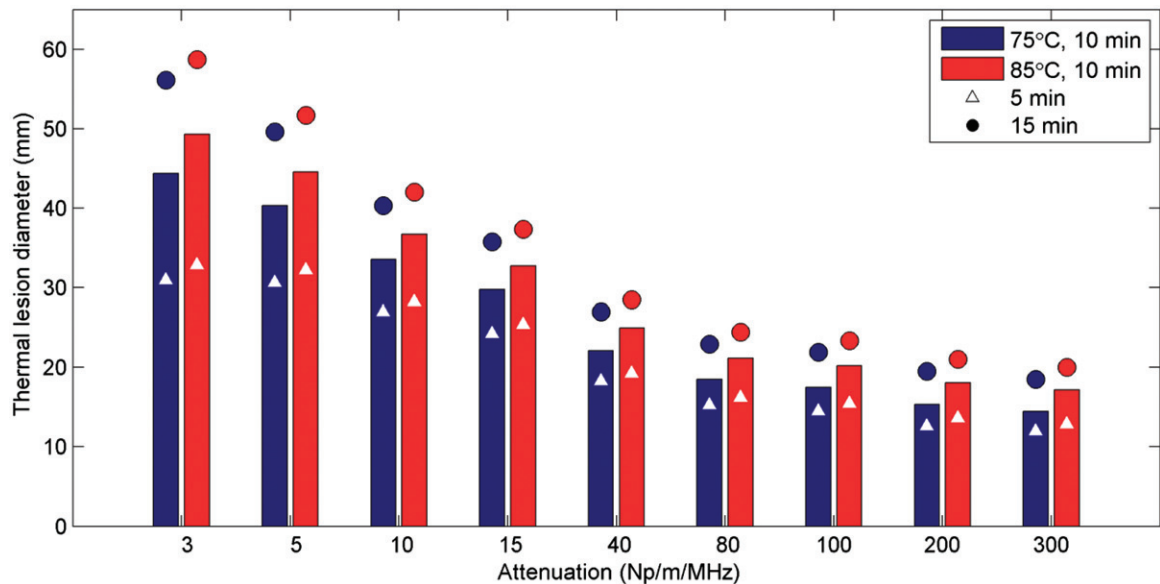


Figure 3. The maximum diameter of tumour tissue that could be ablated in a given time frame was calculated for a variety of ultrasound attenuation coefficients, ablation durations, and control temperatures. Simulations with each tumour attenuation value and each control temperature were performed for ablation durations of 5 min (triangle), 10 min (bar), and 15 min (circle) in a homogenous tissue volume.

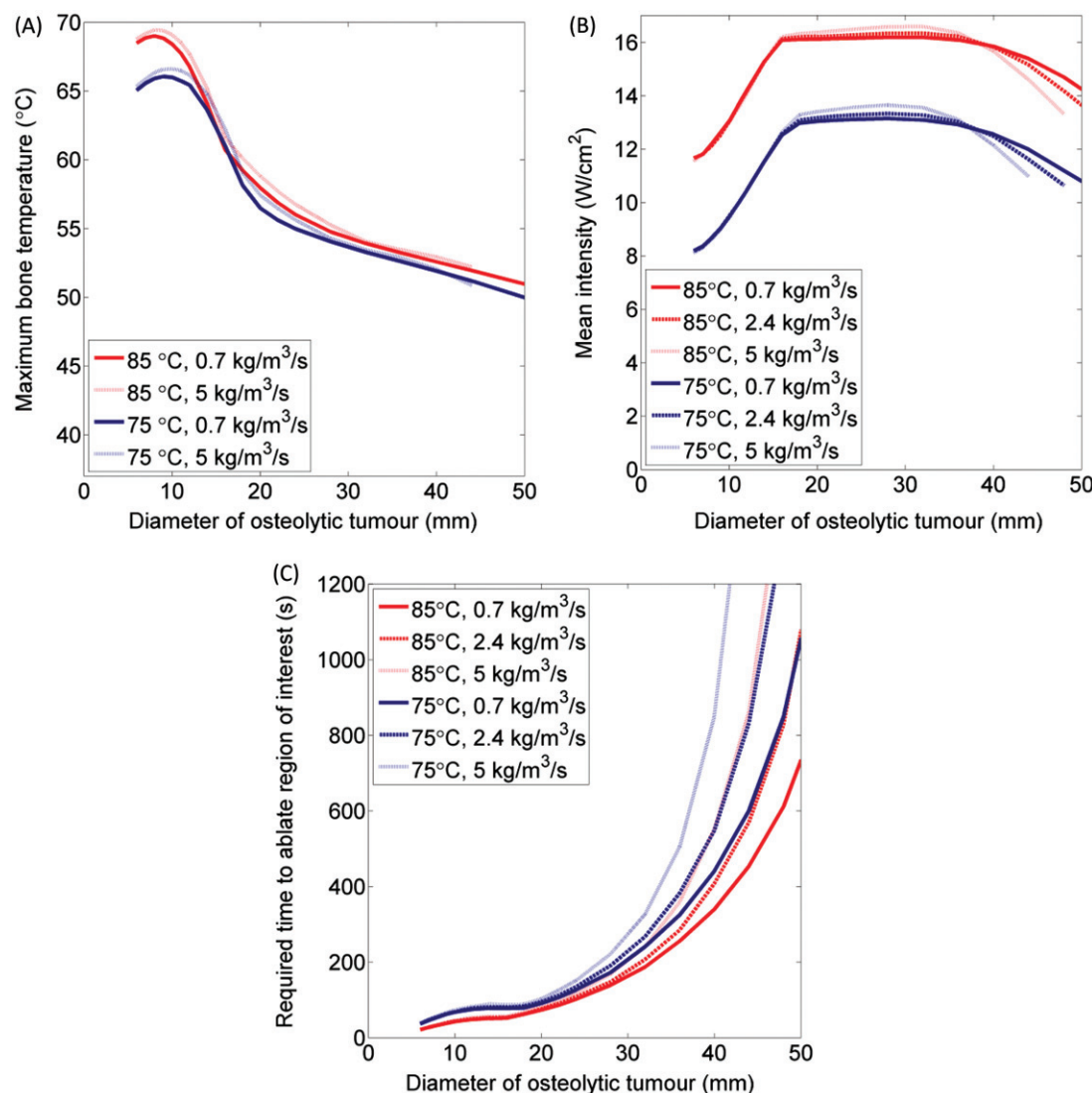


Figure 4. Summary of parametric studies of interstitial ultrasound ablation of a cylindrical tumour volume surrounded by bone: (A) The maximum bone temperature at the time ablation is completed, as a function of tumour diameter, for a variety of blood perfusion rates within the tumour and control temperatures. The mean acoustic intensity, averaged over time (B), and the time necessary (C) to thermally ablate a tumour surrounded by bone are also shown.

resulting bone temperatures (Figure 4). In tumours smaller than 12 mm OD, the temperatures at the bone surfaces were higher than those in the soft tissues closer to the applicator. The bone surfaces were the first portions of the tissues to reach 240 EM43 °C, and then the adjacent soft tissues soon reached lethal temperatures. These tumours were quickly ablated in 21–83 s without reaching the control temperature. Peak bone temperatures (66.8–69.5 °C for an 85 °C set temperature and 6–12 mm OD tumours) varied relatively little with tumour diameter. In 12–16 mm diameter tumours, the bone temperatures were lower in tumours with wider diameters than in narrower tumours (Figure 4A). In tumours with 6–16 mm diameters, the intensities necessary to reach the set temperature increased roughly linearly with the distance between the applicator and the bone (Figure 4B), from 11.7 to 16.1 W/cm² for tumours with 2.4 kg/m³/s perfusion and a control temperature of 85 °C, as more power was necessary to heat bone surfaces further away from the applicator to the control temperature. The necessary

ablation times increased relatively slightly as tumour diameters increased from 6 mm to 16 mm (Figure 4C), from 37 s to 81 s in tumours with 2.4 kg/m³/s perfusion and a set temperature of 75 °C, and from 21 s to 54 s in tumours with a 2.4 kg/m³/s perfusion rate and a set temperature of 85 °C. Up to 14.2% longer ablation durations were required in tumours with higher perfusions, resulting in bone temperatures up to 1.2 °C higher. Otherwise, changes in tumour perfusion had little effect in 6–16 mm OD tumours with low volumes and high bone heating.

In tumours with diameters above 16 mm, peaks in temperature near the applicator were higher than the peaks at the bone surfaces. The maximum temperature, on which the power controller was based, occurred in tumour tissue far from the bone surfaces, and the mean acoustic intensities (Figure 4B) stayed roughly constant as tumour diameters ranged from 16 to 36 mm (12.5–13.7 W/cm² for $T_c = 75$ °C, and 16.1–16.6 W/cm² for $T_c = 85$ °C). The time necessary to ablate tumours over 16 mm in diameter, which had large

volumes and less bone heating than smaller tumours, sharply increased with increasing tumour diameter (Figure 4C), from 52–88 s for 16 mm tumours ($\omega = 0.7\text{--}5\text{ kg/m}^3/\text{s}$, $T_c = 75\text{--}85^\circ\text{C}$) to over 1500 s for very large tumours with high blood perfusion rates ($D \geq 48\text{ mm}$, $T_c = 85^\circ\text{C}$, $\omega = 5\text{ kg/m}^3/\text{s}$). Tumours up to 44–52 mm in diameter ($\omega = 0.7\text{--}5\text{ kg/m}^3/\text{s}$, $T_c = 85^\circ\text{C}$) could be ablated within 900 s. Tumours up to 46–56 mm in diameter ($\omega = 0.7\text{--}5\text{ kg/m}^3/\text{s}$, $T_c = 85^\circ\text{C}$) could be ablated within 1200 s. The applied powers decreased as temperatures approached steady state, reducing the overall mean acoustic intensities applied to ablate large tumours over 32 mm in diameter, by up to 2.1 W/cm^2 for 44 mm tumours. Because the bone/tumour boundaries were the last portions of the tumours over 28 mm in diameter to be ablated, the maximum bone temperatures were $50\text{--}55^\circ\text{C}$, which are those necessary for ablation, with lower temperatures necessary for longer treatment times (Figure 4A). The total amount of acoustic energy delivered could be calculated by multiplying the mean power and treatment time, and ranged from 390–8400 J for tumours 16–44 mm in diameter with blood perfusion rates of $0.7\text{--}5\text{ kg/m}^3/\text{s}$ and set temperatures of 75° or 85°C . In contrast, only 120–520 J was necessary to ablate tumours 6–16 mm in diameter.

The maximum thermal dose in non-targeted nervous tissues was measured for a variety of tumour diameters, set temperatures, and thicknesses of intervening bone and gas (Figure 5). Gaseous insulation between the bone and the nerves was highly effective in protecting nerve tissue, decreasing the thermal dose to the nerves by three orders of magnitude. Insulating bone also had a significant effect on thermal dose to nerves, with bone thicknesses over 4 mm

generally adequate for limiting the thermal dose to nerves to below $6\text{ EM43}^\circ\text{C}$. The thermal dose to nerves increased as a function of tumour diameter when peak temperatures occurred on the bone/tumour interfaces (tumour diameter = $6\text{--}12\text{ mm}$) and when treatment times sharply increased as a function of tumour size (tumour diameter $\geq 20\text{ mm}$). For tumours under 20 mm in diameter, relatively high powers (corresponding to high set temperatures) and short treatment durations produced thermal doses to nerves 1.5–2.3 times lower than low powers and longer treatment durations, and required 13–23% less energy (J). In tumours with diameters of and above 20 mm, the balance between power and time had far fewer effects.

Patient-specific models

Eleven patient-specific models were created to simulate interstitial ultrasound ablation of nine tumours invading paraspinal spaces (case 1), transverse processes (cases 2 and 3), vertebral bodies (cases 4–8), and the ilium (case 9). The percentage of tumour tissue that was ablated, as well as the temperatures and thermal doses in nearby sensitive anatomy, is summarised in Table V for each case. Figures 6–10 show the resulting peak temperature and thermal dose distributions calculated in the target tumour volume and the surrounding 3D tissue volumes. The inner thermal dose contours in 2D images correspond to $240\text{ EM43}^\circ\text{C}$, which is considered a lethal thermal dose [45], and the outer thermal doses contours correspond to $6\text{ EM43}^\circ\text{C}$, a conservative safety margin below which sensitive tissues should be undamaged [30]. All treatment delivery parameters, including the number, length, and sector angle of the

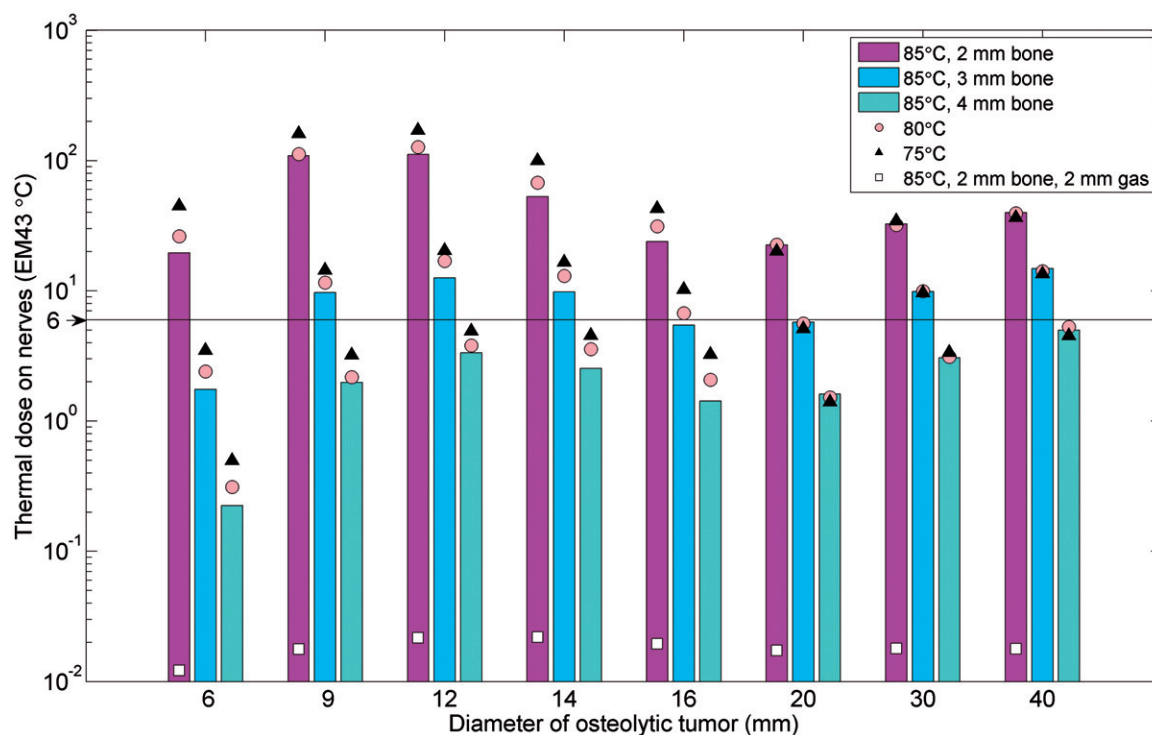


Figure 5. Summary of the maximum thermal dose to nerve tissue adjacent to normal bone encapsulating a tumour (Figure 1) after ablation of the tumour as a function of tumour diameter, bone thicknesses, and control temperature. Each tumour diameter and bone thickness was modelled with control temperatures of 85°C (bar), 80°C (circle), and 75°C (triangle). A case with 2 mm of bone and a 2 mm layer of insulating CO_2 gas was modelled and is shown for comparison. A safety threshold of $6\text{ EM43}^\circ\text{C}$, below which no deleterious effects to nerves are expected, is delineated.

Table V. Treatment parameters and dosimetry results for patient-specific models.

Case	Figure	Sector length and angle	Acoustic intensity (W/cm ²)	Treatment time (s)	% Target ablated	Max temperature and dose on sensitive anatomy, volume canal and nerves over 6 EM43 °C
1	6A, 6B	2 × 1 cm, 360°	10.6	300	100%	SC: 42.1 °C, 0.9 EM43 °C, 0 mm ³
2	6C, 6D	2 × 1 cm, 360°	11.7	300	100%	SC: 38.6 °C, 0.0 EM43 °C, 0 mm ³ Lu: 45.5 °C, 18.7 EM43 °C Ao: 37.0 °C, 0 EM43 °C
3	6E, 6F	2 × 1.5 cm, 180° and 180°	0 and 12.2, 8.1 and 14.9	540	94.6%	SC: 42.2 °C, 1.8 EM43 °C, 0 mm ³
4a	7A, 7B	4 × 1 cm, 360°, CO ₂ insulation	7.8, 9.0, 8.1, 7.1*	520, 640, 380, 190	99.9%	SC: 43.5 °C, 3.1 EM43 °C, 0 mm ³ Ao: 37.1 °C, 0 EM43 °C VC: 37.3 °C, 0 EM43 °C
4b	7C, 7D	4 × 1 cm, 360°, no CO ₂ insulation	7.7, 10.2, 11.9, 8.3*	900, 220, 30, 80	59.7%	SC: 48.1 °C, 12.5 EM43 °C, 3.2 mm ³ Ao: 37.1 °C, 0 EM43 °C VC: 37.3 °C, 0 EM43 °C
5	8A, 8B	1 × 1 cm, 210° and 150°	7.6 and 6.4	230	96.3%	SC: 45.0 °C, 6.9 EM43 °C, 0.03 mm ³ Oe: 37.0 °C, 0 EM43 °C F: 46.2 °C, 15.2 EM43 °C Tr: 37 °C, 0 EM43 °C C: 37.1 °C, 0 EM43 °C
6	8C, 8D	2 × 1.5 cm, 360°	6.2	180	100%	SC: 43.6 °C, 2.5 EM43 °C, 0 mm ³ Ao: 37.4 °C, 0 EM43 °C
7	9A, 9B	2 × 1 cm, 360°	8.6*	600	100%	SC: 39.4 °C, 0.1 EM43 °C, 0 mm ³ Ao: 39.0 °C, 0.1 EM43 °C VC: 37.1 °C, 0 EM43 °C
8	10A–E	1 × 1.5 cm, 180° and 180°	0–15.3 and 9.5–17.8	300	99.9%	SC and N: 44.0 °C, 3.6 EM43 °C, 0 mm ³
9a	10F, 10G	0.5, 1.5, 1.5 cm, 360°, 7 MHz	8.0*	930	100%	N: 39.6 °C, 0.1 EM43 °C, 0 mm ³
9b	10F, 10H	0.5, 1.5, 1.5 cm, 360°, 3 MHz	5.9*	390	100%	N: 39.8 °C, 0.1 EM43 °C, 0 mm ³

SC: Spinal canal, Lu: Lung, Ao: Aorta, VC: Vena cava, Oe: Oesophagus, F: Transverse foramen, Tr: Trachea, C: Carotid artery and internal jugular vein, N: Spinal nerves.

*Time-average of acoustic intensities determined by a feedback controller.

Intensities of two sectors on a single transducer are separated by and. In cases where different intensities and/or ablation durations were applied to different transducers, values are listed in order of distal to proximal transducer segments, and are separated by commas.

transducers as empirically determined, as well as the acoustic intensities and the treatment times, are specified in Table V.

Preferential ultrasound absorption and heating occurred on bone surfaces at the outer boundaries of osteolytic and soft tissue tumours. In cases 1 and 2, in which power was applied uniformly to 360° transducers, simulations showed greater temperature rises in portions of the tumours that were adjacent to bone (Figure 6). To compensate for preferential heating of bone surfaces that were very close to the applicator, which could have caused water vaporisation and/or damage to sensitive tissues, lower powers and/or shorter ablation times were applied to transducer sectors near bone surfaces in cases 3 and 4 (Figures 6 and 7). In case 4, the 360° applicator was not placed in the centre of the tumour, and higher temperatures were calculated on bone surfaces that were closer to the applicator than on bone surfaces that were further away (Figure 7A). To take advantage of preferential ultrasound absorption by bone and to ensure that absorption by bone does not cause any significant portions of the tumour to be shadowed, the applicator was always placed in a location that allows for an acoustic window to all target tissue, such as in the centre of the tumour.

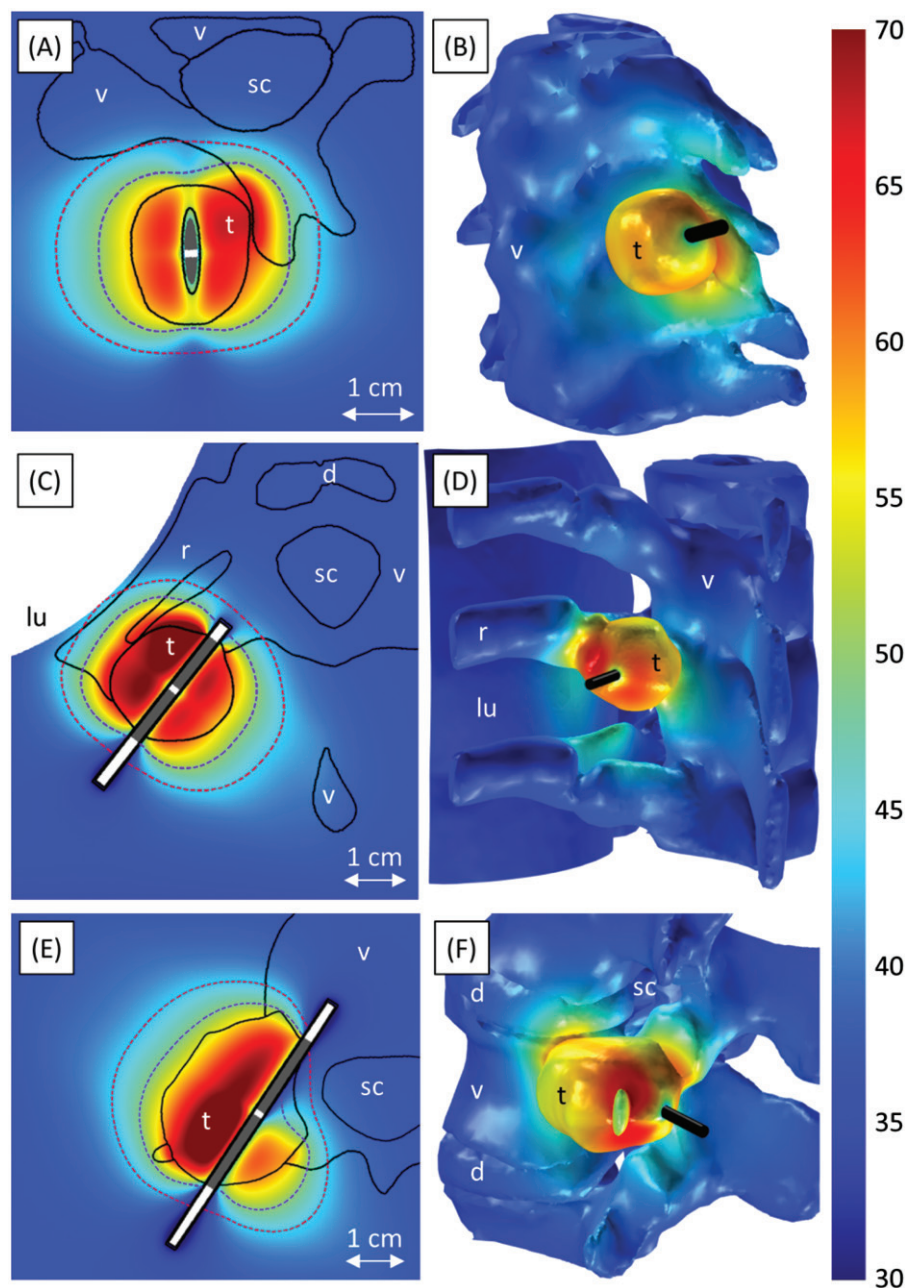
The spinal canal was protected by gaseous dissection in case 4a (Figure 7A and B). A carbon dioxide bubble insulated and displaced the spinal cord from a tumour that invaded the spinal canal. Simulations calculated that 99.9% of the tumour

was ablated, while the spinal cord was protected, with a maximum temperature and thermal dose of 43.5 °C and 3.1 EM43 °C. Without gas present (case 4b, Figures 7C and D), only 59.7% of the tumour could be ablated, and the spinal canal reached 48.1 °C and 12.5 EM43 °C.

The narrow 10–13 mm diameter tumours surrounded by bone that were simulated in cases 5 and 6 (Figure 8) were treated with lower acoustic intensities and ablation durations (6.2–7.6 W/cm², 180–230 s) than other wider tumours treated at 7 MHz (8.0–17.8 W/cm², 300–930 s). The temperatures in cases 5 and 6 peaked in the bone at the tumour boundaries, which heated quickly, rather than immediately adjacent to the applicators. In contrast to cases with longer treatment times and higher powers, in which nearly all tumour tissue was ablated by the end of sonication, the tissue adjacent to the water-cooled catheters in cases 5 and 6 did not reach lethal temperatures during the ablation. However, heat quickly conducted to these narrow regions after power and cooling flow were shut off, ablating the innermost portions of the tumours.

Applicators placed so that the acoustic output would not be directed towards the spinal canal produced little heating in the spinal cord. When the applicator was placed perpendicular to the canal surfaces in cases 1–2 with the transducers 7–14 mm away from them (Figure 6A–D), the spinal canals were heated to only 38.6–42.1 °C and 0.02–0.9 EM43 °C. In case 7, the

Figure 6. Three models of ablation of tumours not encapsulated by bone: adjacent to the cervical vertebrae C4 and C5 in case 1 (A, B), invading the left transverse process of T5 in case 2 (C, D), and invading the left transverse process of L3 in case 3 (E, F). The 240 (violet, inner dashed line) and 6 (crimson, outer dashed line) EM43 °C contours 10 min after treatment are shown atop a colour map of the temperature (°C) at the end of heating in axial slices through the applicator in A, C, and E. 3D temperature maps (°C) at the end of heating are shown on the tumour, bone, intervertebral disc, and spinal canal surfaces in B, D, and F. The position of the transducers, which are skew to the axial plane in A, are shown in grey in A, C, and E, with the whole applicator black in B, D, and F. The locations of the tumour (t), vertebrae (v), spinal canal (sc), intervertebral discs (d), ribs (r), and lung (lu) are indicated.



applicator ran past the spinal canal through the pedicle, and the transducers were positioned so the canal would not be in the direct path of the acoustic energy (Figure 9). The spinal canal, insulated from the tumour by 13 mm of bone, was heated to only 39.4 °C with a maximum thermal dose of 0.1 EM43 °C. Although the 240 EM43 °C contour extended 16.8 mm outward radially from the transducer surface, it only extended 2.8 mm behind the transducer array towards the spinal cord (Figure 9A). Interstitial ultrasound ablation produced well-controlled heating patterns with deep radial penetration through soft tissues and highly osteolytic lesions, and only extending a few millimetres past the lengths of the transducers.

Angularly sectored transducers were used in some cases (3, 5, and 8) to limit heating of the spinal cord. In case 3 and in the last 50 s of case 8, power to the transducer sectors pointing towards the spinal cord was turned off, and power was applied to only one side of the transducer

(Figures 6E and 10D). In case 5, 7.6 W/cm² was applied to the sector directed away from the spinal cord, while 6.4 W/cm² was applied to the sector facing towards the spinal cord (Figure 8A and B). This technique limited the maximum temperature and thermal dose in the spinal canal to 42.2–45.0 °C and 1.8–6.9 EM43 °C.

In case 8, to avoid damage to the right S1 nerve, which exits the posterior sacral foramen less than 4 mm from the posterior portion of the 24-mm long tumour, a single 15-mm long transducer with dual 180° sectors was translated and rotated within the tumour. The anterior portion of the tumour was ablated first (9.5 W/cm², 190 s), followed by the posterior portion (15.3 W/cm², 50 s), with 10 s in between, during which power and flow were shut off (Figure 10B and C). The 30° dead zone between the active sectors was directed towards the nearby sacral canal and foramen to mildly reduce heating of the nerves, with one active sector pointing superior and the other inferior. Greater temperature increases were

Figure 7. Ablation of a tumour invading the vertebral body and spinal canal at level L2. A-B and C-D respectively show ablation with (Case 4a) and without (Case 4b) carbon dioxide injection for tissue dissection and insulation. Colour maps show temperature ($^{\circ}\text{C}$) 190 s into the ablation, before power is shut off to any of the transducers. A and C show temperature in an axial slice through the transducers (grey), with the 240 (violet, inner dashed line) and 6 (crimson, outer dashed line) EM43 $^{\circ}\text{C}$ contours 10 min after treatment superimposed. The applicator (black cylinder) and bone surface (black mesh) are shown in B and D. The locations of the tumour (t), vertebrae (v), spinal canal (sc), intervertebral discs (d), vena cava (vc), and carbon dioxide bubble (CO_2) are indicated.

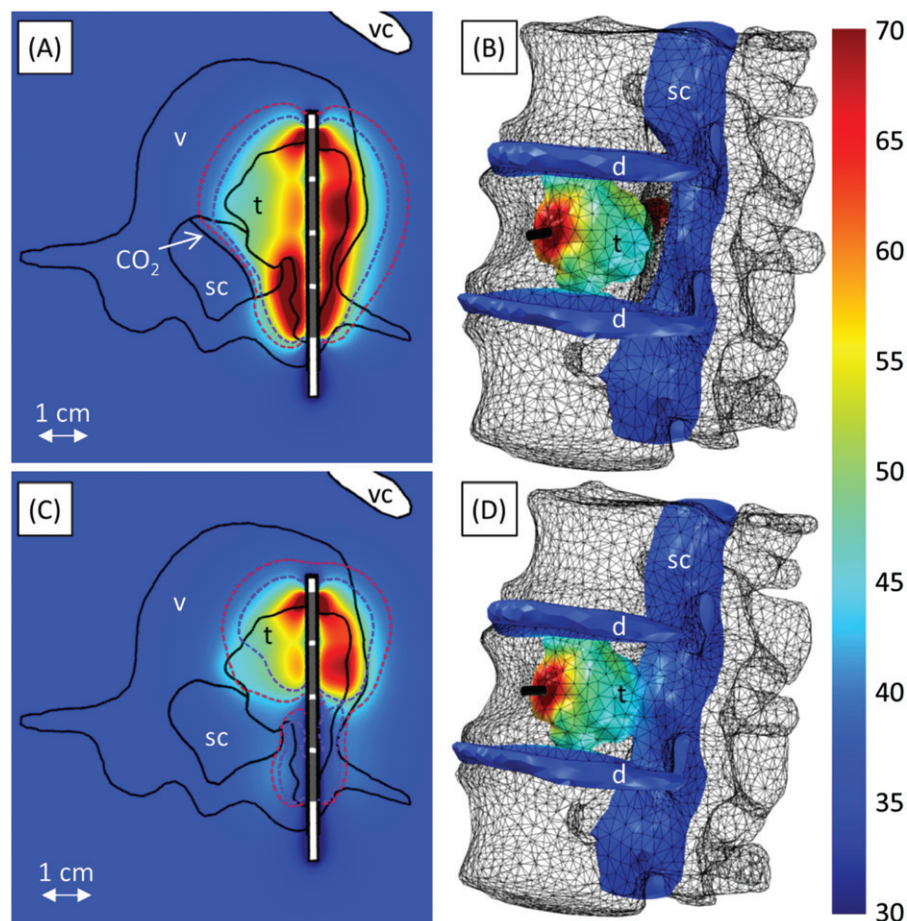


Figure 8. Ablation of narrow osteolytic tumours invading the vertebral bodies of C5 in case 5 (A, B) and L1 in case 6 (C, D). A and C show temperature ($^{\circ}\text{C}$) at the end of heating in vertical slices through the applicator. The 240 (violet, inner dashed line) and 6 (crimson, outer dashed line) EM43 $^{\circ}\text{C}$ contours 10 minutes after treatment, as well as the transducer positions (grey), are also shown. The temperature ($^{\circ}\text{C}$) on the spinal canal, intervertebral discs, and tumour at the end of heating is shown in B and D. A yellow cloud indicates the 240 EM43 $^{\circ}\text{C}$ contour surrounding the tumour (red) 10 min after treatment. The applicator (black cylinder) and bone surface (grey mesh) are also shown. The locations of the tumour (t), vertebrae (v), spinal canal (sc), and intervertebral discs (d) are indicated in the figures.

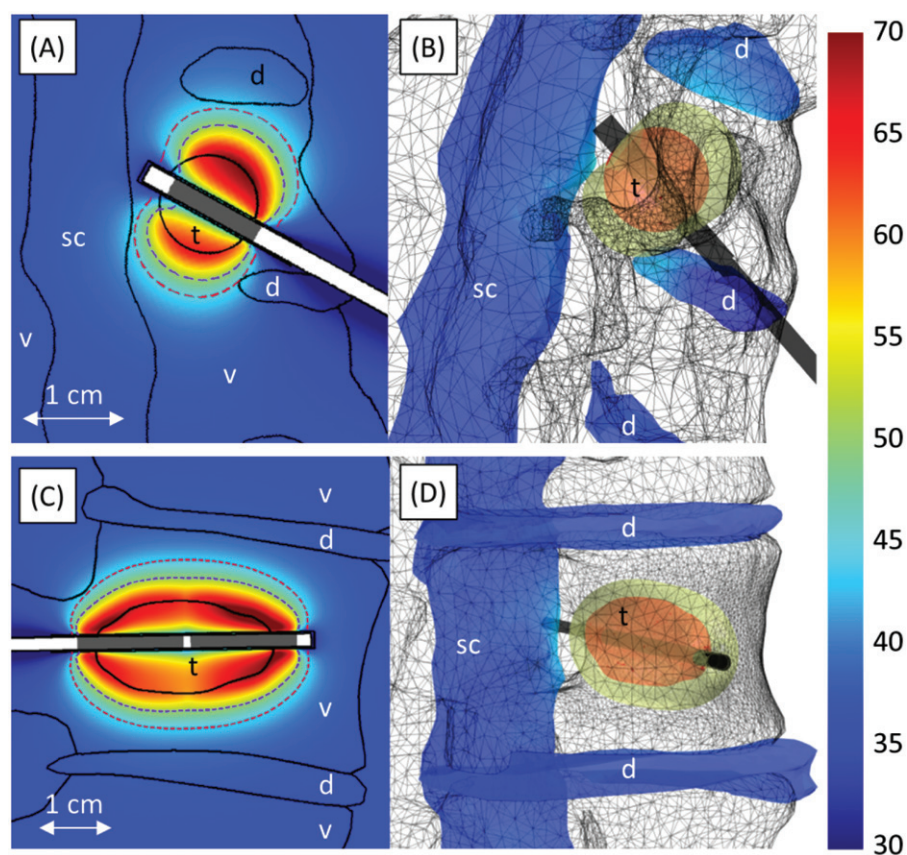


Figure 9. Ablation of an osteolytic tumour invading the anterior portion of the L1 vertebral body (case 7). (A) Temperature ($^{\circ}\text{C}$) at the end of heating in an axial slice through the applicator. The 240 (violet, inner dashed line) and 6 (crimson, outer dashed line) EM43 $^{\circ}\text{C}$ contours 10 min after treatment, as well as transducer positions (grey) are also shown. (B) The temperature ($^{\circ}\text{C}$) on the spinal canal, intervertebral discs, and tumour at the end of heating. The applicator (black cylinder) and bone surface (black mesh) are also shown. The locations of the tumour (t), vertebrae (v), spinal canal (sc), intervertebral discs (d), and aorta (ao) are indicated in the figures.

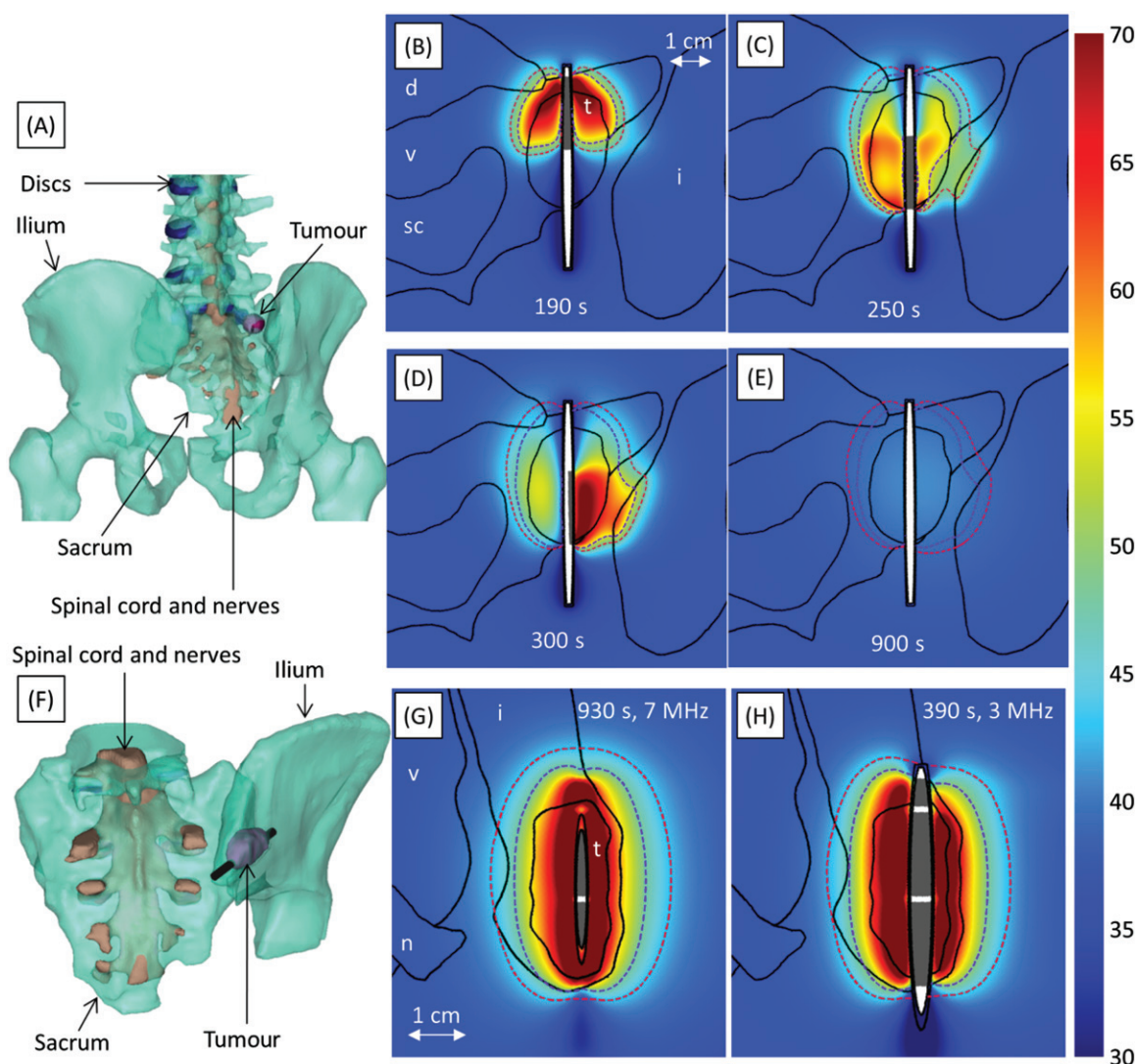
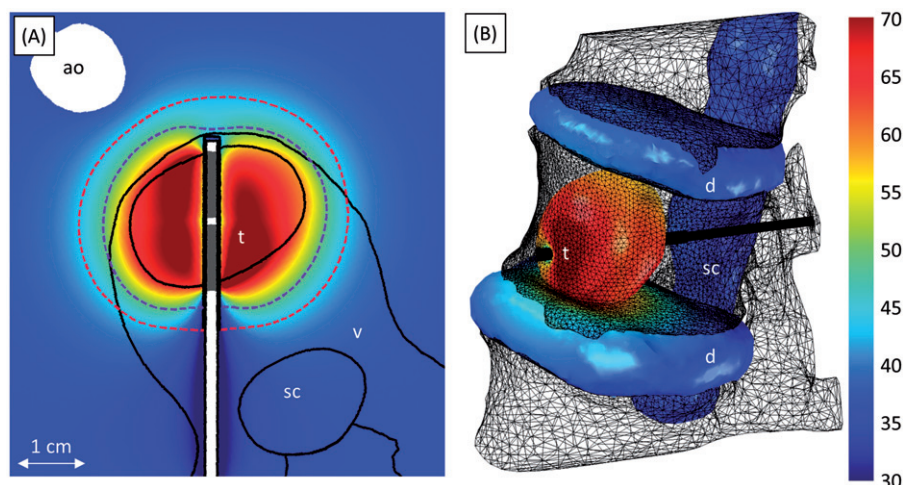


Figure 10. Ablation of tumours near the sacral nerves invading S1 (7 MHz) in case 8 (A–E) and the right iliac bone (3 and 7 MHz) in case 9 (F–H). A and F show the positions of the bones (turquoise), spinal canal (beige), tumour (violet), intervertebral discs (navy blue), and applicator (black). B–E, G, and H show temperature ($^{\circ}\text{C}$) at a given time in axial slices through the applicator. The 240 (violet, inner dashed line) and 6 (crimson, outer dashed line) EM43 $^{\circ}\text{C}$ contours, as well as active transducer positions (grey), at the given time are also shown. The locations of the tumour (t), vertebrae (v), spinal canal (sc), spinal nerves (n), intervertebral discs (d), and ilium (i) are indicated in the figures.

calculated in the left posterior portion of the tumour, which was surrounded by bone and was adjacent to the spinal nerves, than in the right posterior portion of the tumour, which was adjacent to soft tissue. To ablate the right portion of tumour without damaging the spinal nerves to the left, the applicator was rotated. 17.8 W/cm^2 was applied only to the sector pointing right for 50 s, while the sector pointing left was turned off (Figure 10D). These treatment parameters resulted in ablation of nearly the whole volume of the tumour (99.9%), while limiting the thermal dose to the spinal canal and nerves to $3.6 \text{ EM43}^\circ\text{C}$.

In case 9, ablation of a mixed osteolytic and osteoblastic tumour was simulated with 7 MHz and 3 MHz applicators (Figure 10F–H), with applied power regulated by a feedback controller ($T_c = 85^\circ\text{C}$). The 7 MHz applicator, which used lower powers (3.8 W acoustic, as opposed to 5.9 W acoustic) to reach the same temperatures, took more than twice as long (830 s, compared to 290 s) to ablate the full volume. (Since the high frequency transducer had a lower surface area, although the applied powers (W) were lower than at 3 MHz, the surface intensity (W/cm^2) reported in Table V was higher.) Thermal dose contours of $240 \text{ EM43}^\circ\text{C}$ with a wider radial extent were calculated in the 3 MHz case (12.4 mm, 400 s after heating began) than the 7 MHz case (9.0 mm, 400 s after heating began).

Discussion

Parametric and patient-specific FEM biothermal models were created using previously validated methodologies [38,41,47,48] to investigate feasibility and to identify potential treatment delivery strategies for interstitial ultrasound ablation of tumours within and near the spine, through calculation and analysis of approximate temperature and thermal dose distributions. Preferential bone heating, power control along the length and angle of an interstitial ultrasound applicator, and the thermal and acoustic insulation provided by bone can be of particular use for ablation in and near the spine, considering the need for precise heating control in order to protect highly sensitive tissues. Some advantages of interstitial ultrasound, as previously shown in soft tissues, have been demonstrated herein for ablation of spinal and paraspinal tumours: applied powers can be controlled along the length and angle of the applicator to create tailored energy patterns conforming to the target volumes while directing energy away from non-targeted bone and nearby sensitive anatomy, such as nerves. Furthermore, bone adjacent to or surrounding a tumour can augment heating at the tumour boundaries, shortening treatment times while containing heating to the target volume, as bone has a high ultrasound absorption coefficient and is thermally and acoustically insulating. Given these attributes, interstitial ultrasound ablation appears feasible to treat soft tissue tumours adjacent to bone and highly osteolytic tumours within bone up to 44–52 mm OD. Moreover, tumours within 4–5 mm of the spinal canal may possibly be ablated while maintaining safe thermal dose exposures to nerve tissue in cases with 4–5 mm thicknesses of normal intervening bone, tailored directional heating patterns, and/or carbon dioxide dissection.

The impact of bone tissue is considerable on the performance of interstitial ultrasound, and it has a significant role in thermal dosimetry and treatment outcomes. Normal bone has an ultrasound absorption coefficient one to two orders of magnitude higher than that of unossified tissues [35]. At 7 MHz, most of the acoustic energy transmitted into bone is absorbed within 1–3 mm of the bone surface, thereby limiting further penetration (acoustic insulation) and producing considerable power deposition localised at the bone/soft tissue interface, which can increase heating at the boundaries of tumours adjacent to bone. Bone also has a lower thermal conductivity than soft tissue, providing a modestly increased thermal resistance or insulating effect. In contrast, osteoblastic (high bone content) tumours have high acoustic attenuations, which can negatively impact acoustic penetration and the maximum temperatures achievable with interstitial ultrasound.

Parametric and patient-specific simulations indicate that osteolytic tumours up to 40–47 mm in diameter surrounded by bone can be ablated within 10 min (Figure 4C), and that diameters up to approximately 46–56 mm can be ablated with longer durations approaching 20 min. Limiting applied acoustic intensities to 13.7 or 16.6 W/cm^2 in order to not surpass maximum temperatures of 75° or 85°C , respectively, and to avoid boiling resulted in large increases in the time necessary to treat large tumours. These achievable target dimensions are similar to those that can be treated with RF, laser, and cryoablation, and the treatment times are similar to or shorter than those of these other modalities [20,23,56].

Interstitial ultrasound ablation at 7 MHz is best suited for the ablation of highly osteolytic lesions. However, for tumours with high bone content and attenuations over 80 Np/m/MHz (Figure 3), decreased acoustic penetration causes high temperature rises very close to the applicator, limiting the powers that can be applied. Long ablation durations, as in case 9a (Figure 10G), are necessary for 7 MHz ablation of permeative, mixed, or osteoblastic lesions, which, due to their higher bone content, are likely to have high ultrasound attenuation coefficients. Although an exact measurement of tumour attenuation may be difficult to obtain in clinical cases, CT scans or histology studies of tumours may provide information on bone content, based upon which acoustic attenuation may be estimated [57]. Further studies of the relationship between the two, as well as closed-loop power control, may be necessary if the models are revised for clinical applications. Conduction dominates heating of the outer portions of tumours with attenuations of $80\text{--}300 \text{ Np/m/MHz}$, such that 20–24 mm diameters can be treated at 7 MHz in 15 min (Figure 3). Alternatively, ablation can be performed at 3 MHz with shorter ablation durations, as in case 9b, because greater penetration into bone at lower frequencies allows for the use of higher powers without the risk of water vaporisation in tissue (Table V, Figure 10H). To accommodate the thicker transducers needed to produce longer wavelengths, 3 MHz applicators have larger diameters than 7 MHz applicators. The diameters of the 3 MHz applicators considered are similar to some of those used in vertebroplasty, such as the KyphX system which requires a 4.2 mm cannula (Medtronic, Minneapolis, MN).

Patient-specific models demonstrated the feasibility of interstitial ultrasound ablation of tumours in and near the spine, with complete ablation of five tumours at least 4.3 mm from the spinal canal, and ablation of 94.6–100% of the volumes of four tumours within 4.5 mm of the spinal canal (Table V). This patient-specific study indicates that tumours at least 5 mm from the sensitive neural elements can be fully treated with interstitial ultrasound ablation without the need for gaseous insulation. However, parametric studies determined that 4 mm of bone surrounding round tumours may be sufficient to insulate nervous structures, with 3 mm of bone sufficient in tumours 16–20 mm in diameter or under 6 mm in diameter (Figure 5). Thicker bone insulation was required in some patient-specific models most likely because the tumours were irregularly shaped. When one portion of a tumour is wider than another, such as the tumour 4.5 mm from the spinal canal in case 3 (Figure 6E and F), the higher powers necessary to ablate the wide portion may overheat parts of the spinal canal near a narrow portion. In such cases, additional nervous protection, such as gaseous dissection or reduced energy directed towards the nerves, may be required in order to ablate the full tumour volume.

A variety of techniques were found to potentially protect sensitive anatomy. The critical anatomy in the vicinity of the spine includes the spinal cord, spinal nerves, aorta, vena cava, oesophagus, trachea, and lungs. Less or no power can be delivered to transducer sectors directed towards the spinal cord, nerve roots, or other sensitive tissues, as in cases 3, 4, 5, and 8 (Figures 6, 7, 8A and B, 10A–E). In these cases, the sector angles of the transducers were selected and aimed so that highly heated areas such as sonicated bone surfaces were at least 3–4 mm from tissue to be preserved. The number and length of the transducers can be selected so that the transducer array extends beyond the full length of the tumour, and so that individual transducer sectors are aligned with any volumes to receive less energy (cases 1–9). The applicator can be placed near critical structures, and all power can be directed away from them, as in Figure 6(E). Alternatively, a transducer can be translated and/or rotated to ablate a target volume while limiting heating of sensitive structures (Figure 10A–E). Gaseous dissection can be applied to thermally and acoustically insulate vital neurological structures, which is particularly necessary if there is less than 4–5 mm of healthy bone to insulate them (Figure 7).

Small osteolytic tumours under 16 mm in diameter were best heated with fast ablations and high intensities rather than relatively slowly with low intensities in order to protect sensitive tissues nearby (Figure 5). These small tumours heat quickly because of the high temperature peaks at the nearby tumour/bone boundaries (Figure 4A). When the tumours were heated relatively slowly, simulations showed damage to nearby nerves (Figure 5), due in part to thermal conduction from the highly heated bone surfaces over time and because slower ablations with lower powers required more energy.

The directionality and minimally invasive nature of interstitial ultrasound ablation provides it with some benefits as compared to other ablative modalities, while allowing it to take advantage of techniques used with the other modalities. Other ablation modalities used in the spine lack directional control. To protect the spinal cord, they rely solely on cortical

bone insulation, the cooling flow of blood and CSF, and/or carbon dioxide dissection [18,20,23,31], which can also supplement protection of sensitive tissues during interstitial ultrasound ablation. Unlike HIFU, which requires an acoustic window to a large external transducer, interstitial ultrasound can treat tumours enclosed within bone (Figures 7–10). A single interstitial ultrasound applicator with variable power control to four 1 cm long transducers may treat the entire length of a 43 mm long tumour at once (Table V, Figure 7A and B). In contrast, RF electrodes with short (1 cm) active tips need to be used in many cases to prevent neurological damage [58]. As with other ablative modalities [24,59], an interstitial ultrasound applicator can be repositioned within a tumour and multiple applicators can be used simultaneously in order to ablate larger volumes. Applicator placement and gaseous dissection for neural protection can be performed following methodologies already in place for RF and laser ablation procedures in the spine [16,17,21,23,31].

Development of an accurate and fast treatment planning platform is challenging for thermal therapy technologies in general, due to computational complexity and heterogeneous and often unknown tissue and tumour properties [60–64]. The patient-specific models generated in this work were used to estimate temperature and thermal dose distributions produced by interstitial ultrasound in a variety of generalised cases and representative patient anatomies, with a focus on exploring trends, delivery strategies, and potential for use, but not directly for treatment planning. Improvements in model accuracy for future patient-specific treatment planning applications could potentially be attained through determination of the attenuation coefficient of the tumours, especially those with variable bone content. It may be difficult to obtain an exact measurement of tumour attenuation in clinical cases; however, CT scans or histological data may provide information on bone content, based upon which acoustic attenuation may be estimated [57,65]. In addition, *in situ* measurements of tissue properties such as thermal conductivity and perfusion could also improve model accuracy [60,66]. Further, models in treatment plans could incorporate acoustic output characteristics specific to individual applicators, which would be measured in routine quality assurance analysis. Computational challenges and complexities encountered in treatment planning could potentially be addressed through incorporation of simplifying approximations or assumptions into the modelling framework [61–63].

As demonstrated in this study, clinical implementation of interstitial ultrasound ablation in and around the spine can be complex, considering the dramatically different treatment scenarios which may be encountered. Additionally, the spatial and dynamic control of heating associated with interstitial ultrasound technology can provide significant advantages in this setting, but can also increase the complexity of treatment delivery and treatment planning. To improve the speed and practicality of the treatment planning process, practical selection of applicator position and the length, number, and angular extent of transducer sectors could be determined a priori based solely on geometric considerations from diagnostic images, to reflect the tumour dimensions relative to the applicator axis with separate sectors aligned with targeted and untargeted tissue. Further, optimal treatment delivery

parameters (e.g. power, duration) could be determined for a variety of ‘standard’ cases using a combination of theoretical modelling, optimisation algorithms, and parametric studies, along with ex vivo and in vivo performance studies. Following clinical procedures typically used for RF and microwave ablation, look-up tables based upon this data could inform selection of applied power levels and treatment durations, depending upon the tumour dimensions and other parameters. Fast methods of optimisation-based 3D patient-specific planning, such as those that employ specific absorption rate or temperature superposition, or estimation of tissue properties based on measured temperature changes, could possibly be employed to determine treatment parameters such as input power levels, applicator positions, transducer dimensions, and directivity [49,67–74]. Ultimately, image-guided placement combined with real-time closed loop control based on invasive temperature measurements or MRTI could be utilised to compensate for any treatment planning limitations and for dynamic tissue changes to obtain the best possible treatment.

Conclusion

Parametric and patient-specific studies have demonstrated the capability of interstitial ultrasound ablation to create thermal lesions conforming to the shapes of tumours in and near the spine while preserving neighbouring critical anatomical structures. Preferential acoustic absorption at bone surfaces results in additional heating at the boundaries of tumours adjacent to bone, enhancing and accelerating ablation. Larger 3 MHz transducers may be used to treat tumours with attenuations higher than those of soft tissues. Interstitial ultrasound ablation appears feasible for the complete ablation of tumours at least 4–5 mm from critical neural structures. To safely ablate all or part of tumours 0–5 mm from the spinal canal and nerves, sensitive anatomy may be maintained at safe temperatures though carbon dioxide dissection and/or through control of power along the length and angle of the applicator, so that little or no energy is directed towards critical structures.

Declaration of interest

We gratefully acknowledge support by the National Institutes of Health grants R44CA112852 and P01 CA159992. This work is a collaboration between the University of California, San Francisco and Acoustic MedSystems supported by a Small Business Industry Research grant from the National Institutes of Health. E. Clif Burdette is affiliated with Acoustic MedSystems, which has a commercial interest in interstitial ultrasound technology. The authors alone are responsible for the content and writing of the paper.

References

- Coleman R. Metastatic bone disease: Clinical features, pathophysiology and treatment strategies. *Cancer Treat Rev* 2001;27:165–76.
- Wong DA, Fornasier VL, MacNab I. Spinal metastases: The obvious, the occult, and the impostors. *Spine* 1990;15:1–4.
- SEER Cancer Statistics Review, 1975–2009 (Vintage 2009 populations). In: Howlander N, Noone AM, Krapcho M, Neyman N, Aminou R, Altekruse SF, et al., eds. Bethesda, MD: National Cancer Institute, 2012.
- Park KY, Shin DA, Shin HC, Yoon DH, Kim KN. Surgical management of paraspinal tumors. *Kor J Spine* 2007;4:134–9.
- Longhi A, Errani C, Paolisi MD, Mercuri M, Baccia G. Primary bone osteosarcoma in the pediatric age: State of the art. *Cancer Treat Rev* 2006;32:423–36.
- Nagarajan R, Neglia JP, Clohisy DR, Robison LL. Limb salvage and amputation in survivors of pediatric lower-extremity bone tumors: What are the long-term implications? *J Clin Oncol* 2002;20:4493–501.
- Sciubba DM, Petteys RJ, Dekutoski MB, Fisher CG, Fehlings MG, Ondra SL, et al. Diagnosis and management of metastatic spine disease: A review. *J Neurosurg Spine* 2010;13:94–108.
- Rosenthal D, Callstrom MR. Critical review and state of the art in interventional oncology: Benign and metastatic disease involving bone. *Radiology* 2012;262:765–80.
- Callstrom MR, Charboneau JW, Goetz MP, Rubin J, Atwell TD, Farrell MA, et al. Image-guided ablation of painful metastatic bone tumors: A new and effective approach to a difficult problem. *Skeletal Radiol* 2006;35:1–15.
- Cantwell CP, Obyrne J, Eustace S. Current trends in treatment of osteoid osteoma with an emphasis on radiofrequency ablation. *Eur Radiol* 2004;14:607–17.
- Schwab JH, Springfield DS, Raskin KA, Mankin HJ, Hornicek FJ. What's new in primary bone tumors. *J Bone Joint Surg Am* 2012;94:1913–19.
- Terezakis SA, Lovelock DM, Bilsky MH, Hunt MA, Zatzky J, Yamada Y. Image-guided intensity-modulated photon radiotherapy using multifractionated regimen to paraspinal chordomas and rare sarcomas. *Int J Radiat Oncol Biol Phys* 2007;69:1502–8.
- Weber DC, Trofimov AV, Delaney TF, Bortfeld T. A treatment planning comparison of intensity modulated photon and proton therapy for paraspinal sarcomas. *Int J Radiat Oncol Biol Phys* 2004;58:1596–606.
- Kurup AN, Callstrom MR. Ablation of skeletal metastases: Current status. *J Vasc Interv Radiol* 2010;21:S242–50.
- Martel J, Bueno Á, Nieto-Morales ML, Ortiz EJ. Osteoid osteoma of the spine: CT-guided monopolar radiofrequency ablation. *Eur J Radiol* 2009;71:564–9.
- van der Linden E, Kroft LJ, Dijkstra P. Treatment of vertebral tumor with posterior wall defect using image-guided radiofrequency ablation combined with vertebroplasty: Preliminary results in 12 patients. *J Vasc Interv Radiol* 2007;18:741–7.
- Katonis P, Pasku D, Alpantaki K, Bano A, Tzanakakis G, Karantanis A. Treatment of pathologic spinal fractures with combined radiofrequency ablation and balloon kyphoplasty. *World J Surg Oncol* 2009;7:90.
- Dupuy DE, Hong R, Oliver B, Goldberg SN. Radiofrequency ablation of spinal tumors: Temperature distribution in the spinal canal. *Am J Roentgenol* 2000;175:1263–6.
- Gangi A, Basile A, Buy X, Alizadeh H, Sauer B, Bierry G. Radiofrequency and laser ablation of spinal lesions. *Seminars in Ultrasound, CT, and MRI* 2005;26:89–97.
- Vanderschueren GM, Obermann WR, Dijkstra SP, Taminiau AH, Bloem JL, van Erkel AR. Radiofrequency ablation of spinal osteoid osteoma: Clinical outcome. *Spine* 2009;34:901–3.
- Georgy B. Bone cement deposition patterns with plasma-mediated radio-frequency ablation and cement augmentation for advanced metastatic spine lesions. *Am J Neuroradiol* 2009;30:1197–202.
- Carrafiello G, Laganà D, Pellegrino C, Fontana F, Mangini M, Nicotera P, et al. Percutaneous imaging-guided ablation therapies in the treatment of symptomatic bone metastases: Preliminary experience. *Radiol Med* 2009;114:608–25.
- Rybak LD, Gangi A, Buy X, Vieira RLR, Wittig J. Thermal ablation of spinal osteoid osteomas close to neural elements: Technical considerations. *Am J Roentgenol* 2010;195:W293–8.
- Pusceddu C, Sotgia B, Fele RM, Melis L. Treatment of bone metastases with microwave thermal ablation. *J Vasc Interv Radiol* 2012;24:229–33.
- Tsoumakidou G, Garnon J, Ramamurthy N, Buy X, Gangi A. Interest of electrostimulation of peripheral motor nerves during percutaneous thermal ablation. *Cardiovasc Intervent Radiol* 2013;36:1624–8.
- Catane R, Beck A, Inbar Y, Rabin R, Shabshin N, Hengst S, et al. MR-guided focused ultrasound surgery (MRgFUS) for the

- palliation of pain in patients with bone metastases – Preliminary clinical experience. *Ann Oncol* 2007;18:163–7.
27. Liberman B, Gianfelice D, Inbar Y, Beck A, Rabin T, Shabshin N, et al. Pain palliation in patients with bone metastases using MR-guided focused ultrasound surgery: A multicenter study. *Ann Surg Oncol* 2009;16:140–6.
 28. Wang Y, Wang W, Tang J. Primary malignant tumours of the bony pelvis: US-guided high intensity focused ultrasound ablation. *Int J Hyperthermia* 2013;29:683–7.
 29. Anis N, Chawki N, Antoine K. Use of radio-frequency ablation for the palliative treatment of sacral chordoma. *Am J Neuroradiol* 2004;25:1589–91.
 30. Haveman J, Sminia P, Wondergem J, Van Der Zee J, Hulshof M. Effects of hyperthermia on the central nervous system: What was learnt from animal studies? *Int J Hyperthermia* 2005;21:473–87.
 31. Buy X, Tok C-H, Szwarc D, Bierry G, Gangi A. Thermal protection during percutaneous thermal ablation procedures: Interest of carbon dioxide dissection and temperature monitoring. *Cardiovasc Intervent Radiol* 2009;32:529–34.
 32. Scott SJ, Prakash P, Salgaonkar V, Jones PD, Cam RN, Han M, et al. Interstitial ultrasound ablation of tumors within or adjacent to bone: Contributions of preferential heating at the bone surface. *Proc SPIE* 2013;8584:85840Z. doi:10.1117/12.2002632.
 33. Sciubba DM, Burdette EC, Cheng JJ, Pennant WA, Noggle JC, Petteys RJ, et al. Percutaneous computed tomography fluoroscopy-guided conformal ultrasonic ablation of vertebral tumors in a rabbit tumor model: Laboratory investigation. *J Neurosurg Spine* 2010;13:733–79.
 34. Nau WH, Diederich CJ, Burdette EC. Evaluation of multielement catheter-cooled interstitial ultrasound applicators for high-temperature thermal therapy. *Med Phys* 2001;28:1525–34.
 35. Duck F. *Physical Properties of Tissue: A Comprehensive Reference Book*. London: Academic Press, 1990.
 36. Fujii M, Sakamoto K, Toda Y, Negishi A, Kanai H. Study of the cause of the temperature rise at the muscle–bone interface during ultrasound hyperthermia. *IEEE Trans Biomed Eng* 1999;46:494–504.
 37. Moros EG, Novak P, Straube WL, Kolluri P, Yablonskiy DA, Myerson RJ. Thermal contribution of compact bone to intervening tissue-like media exposed to planar ultrasound. *Phys Med Biol* 2004;49:869–86.
 38. Scott SJ, Prakash P, Salgaonkar V, Jones PD, Cam RN, Han M, et al. Approaches for modeling interstitial ultrasound ablation of tumors within or adjacent to bone: Theoretical and experimental evaluations. *Int J Hyperthermia* 2013;29:629–42.
 39. Nau WH, Diederich CJ, Ross AB, Butts K, Rieke V, Bouley DM, et al. MRI-guided interstitial ultrasound thermal therapy of the prostate: A feasibility study in the canine model. *Med Phys* 2005;32:733–43.
 40. Diederich CJ. Ultrasound applicators with integrated catheter-cooling for interstitial hyperthermia: Theory and preliminary experiments. *Int J Hyperthermia* 1996;12:279–97.
 41. Diederich CJ, Hynynen K. Induction of hyperthermia using an intracavitary multielement ultrasonic applicator. *IEEE Trans Biomed Eng* 1989;36:432–8.
 42. Tyr  us PD, Nau WH, Diederich CJ. Effect of applicator diameter on lesion size from high temperature interstitial ultrasound thermal therapy. *Med Phys* 2003;30:1855–63.
 43. Pennes HH. Analysis of tissue and arterial blood temperatures in the resting human forearm. *J Appl Physiol* 1948;1:93–122.
 44. Sapareto SA, Dewey WC. Thermal dose determination in cancer therapy. *Int J Radiat Oncol Biol Phys* 1984;10:787–800.
 45. Dewey WC. Arrhenius relationships from the molecule and cell to the clinic. *Int J Hyperthermia* 1994;10:457–83.
 46. Prakash P, Diederich CJ. Considerations for theoretical modelling of thermal ablation with catheter-based ultrasonic sources: Implications for treatment planning, monitoring and control. *Int J Hyperthermia* 2012;28:69–86.
 47. Prakash P, Salgaonkar VA, Cliff Burdette E, Diederich CJ. Multiple applicator hepatic ablation with interstitial ultrasound devices: Theoretical and experimental investigation. *Med Phys* 2012;39:7338–49.
 48. Tyr  us PD, Diederich CJ. Theoretical model of internally cooled interstitial ultrasound applicators for thermal therapy. *Phys Med Biol* 2002;47:1073–89.
 49. Chen X, Diederich CJ, Wootton JH, Pouliot J, Hsu I-C. Optimisation-based thermal treatment planning for catheter-based ultrasound hyperthermia. *Int J Hyperthermia* 2010;26:39–55.
 50. Schaefer O, Lohrmann C, Markmiller M, Uhrmeister P, Langer M. Combined treatment of a spinal metastasis with radiofrequency heat ablation and vertebroplasty. *Am J Roentgenol* 2003;180:1075–7.
 51. Sutphen SA, Murakami JW. Radiofrequency ablation of a cervical osteoid osteoma: A trans-thyroid approach. *Pediatr Radiol* 2007;37:83–5.
 52. Tateishi U, Gamez C, Dawood S, Yeung HWD, Cristofanilli M, Macapinlac HA. Bone metastases in patients with metastatic breast cancer: Morphologic and metabolic monitoring of response to systemic therapy with integrated PET/CT1. *Radiology* 2008;247:189–96.
 53. Costelloe CM, Chuang HH, Madewell JE, Ueno NT. Cancer response criteria and bone metastases: RECIST 1.1, MDA and PERCIST. *J Cancer* 2010;1:80–92.
 54. Debnam JM, Guha-Thakurta N, Mahfouz YM, Garden AS, Benjamin RS, Sturgis EM, et al. Radiation-associated head and neck sarcomas: Spectrum of imaging findings. *Oral Oncol* 2012;48:155–61.
 55. Diederich C, Nau W, Ross A, Tyreus P, Butts K, Rieke V, et al. Catheter-based ultrasound applicators for selective thermal ablation: Progress towards MRI-guided applications in prostate. *Int J Hyperthermia* 2004;20:739–56.
 56. Masala S, Roselli M, Manenti G, Mammucari M, Bartolucci DA, Simonetti G. Percutaneous cryoablation and vertebroplasty: A case report. *Cardiovasc Intervent Radiol* 2008;31:669–72.
 57. Hakulinen MA, Day JS, T  yr  s J, Weinans H, Jurvelin JS. Ultrasonic characterization of human trabecular bone microstructure. *Phys Med Biol* 2006;51:1633–48.
 58. Adachi A, Kaminou T, Ogawa T, Kawai T, Takaki Y, Sugiura K, et al. Heat in spinal canal during radiofrequency ablation for vertebral lesions: Study in swine. *Radiology* 2008;247:374–80.
 59. Claren  on F, Jean B, Pham H-P, Cormier E, Bensimon G, Rose M, et al. Value of percutaneous radiofrequency ablation with or without percutaneous vertebroplasty for pain relief and functional recovery in painful bone metastases. *Skeletal Radiol* 2013;42:25–36.
 60. Raaymakers B, Van Vulpen M, Lagendijk J, De Leeuw A, Crezee J, Battermann J. Determination and validation of the actual 3D temperature distribution during interstitial hyperthermia of prostate carcinoma. *Phys Med Biol* 2001;46:3115–31.
 61. Paulides MM, Stauffer PR, Neufeld E, Maccarini PF, Kyriakou A, Canters RA, et al. Simulation techniques in hyperthermia treatment planning. *Int J Hyperthermia* 2013;29:346–57.
 62. Prakash P, Salgaonkar VA, Diederich CJ. Modelling of endoluminal and interstitial ultrasound hyperthermia and thermal ablation: Applications for device design, feedback control and treatment planning. *Int J Hyperthermia* 2013;29:296–307.
 63. Feng Y, Fuentes D. Model-based planning and real-time predictive control for laser-induced thermal therapy. *Int J Hyperthermia* 2011;27:751–61.
 64. Lagendijk J. Hyperthermia treatment planning. *Phys Med Biol* 2000;45:R61–R76.
 65. Laugier P, Droin P, Laval-Jeantet A, Berger G. In vitro assessment of the relationship between acoustic properties and bone mass density of the calcaneus by comparison of ultrasound parametric imaging and quantitative computed tomography. *Bone* 1997;20:157–65.
 66. Haase S, Patz T, Tiesler H, Altrogge I, Preusser T. Radiofrequency ablation planning beyond simulation. *Engineering in Medicine and Biology Society (EMBC), 2012 Annual International Conference of the IEEE, 2012*, 191–4.
 67. Sommer CM, Sommer SA, Sommer WO, Zelzer S, Wolf MB, Bellemann N, et al. Optimisation of the coagulation zone for thermal ablation procedures: A theoretical approach with considerations for practical use. *Int J Hyperthermia* 2013;29:620–8.
 68. Salgaonkar VA, Prakash P, Diederich CJ. Temperature superposition for fast computation of 3D temperature distributions during optimization and planning of interstitial ultrasound hyperthermia treatments. *Int J Hyperthermia* 2012;28:235–49.
 69. Cheng K-S, Stakhursky V, Craciunescu OI, Stauffer P, Dewhirst M, Das SK. Fast temperature optimization of multi-source

- hyperthermia applicators with reduced-order modeling of 'virtual sources'. *Phys Med Biol* 2008;53:1619–35.
70. Kok H, van den Berg C, Bel A, Crezee J. Fast thermal simulations and temperature optimization for hyperthermia treatment planning, including realistic 3D vessel networks. *Med Phys* 2013;40:103303.
 71. Altrogge I, Preusser T, Kroger T, Haase S, Patz T, Kirby M. Sensitivity analysis for the optimization of radiofrequency ablation in the presence of material parameter uncertainty. *Int J Uncertain Quantif* 2012;2:295–321.
 72. Altrogge I, Preusser T, Kröger T, Büskens C, Pereira PL, Schmidt D, et al. Multiscale optimization of the probe placement for radiofrequency ablation. *Acad Radiol* 2007;14:1310–24.
 73. Oden JT, Diller K, Bajaj C, Browne J, Hazle J, Babuška I, et al. Dynamic data-driven finite element models for laser treatment of cancer. *Numerical methods for partial differential equations* 2007; 23:904–22.
 74. Khalil-Bustany I, Diederich C, Polak E, Kirjner-Neto C. Minimax optimization-based inverse treatment planning for interstitial thermal therapy. *Int J Hyperthermia* 1998;14:347–66.
 75. Damianou C, Sanghvi N, Fry F. Dependence of ultrasonic attenuation and absorption in dog soft tissues on temperature and thermal dose. *J Acoust Soc Am* 1997;102:628–34.
 76. Williams LR, Leggett RW. Reference values for resting blood flow to organs of man. *Clin Phys Physiol Meas* 1989;10:187–217.
 77. Haws CW, Heistad DD. Effects of nimodipine on cerebral vasoconstrictor responses. *Am J Physiol Heart Circ Physiol* 1984; 247:H170–6.
 78. Töyräs J, Laasanen MS, Saarakkala S, Lammi MJ, Rieppo J, Kurkijärvi J, et al. Speed of sound in normal and degenerated bovine articular cartilage. *Ultrasound Med Biol* 2003;29:447–54.
 79. Sierra G, Leung M, Le Guyader P, Savard P. Thermal and electrical characterization of the intervertebral disc. *Proc 25th Ann Int Conf IEEE Eng Med Biol Soc* 2003;4:3035–6.
 80. Urban JPG, Smith S, Fairbank JCT. Nutrition of the intervertebral disc. *Spine* 2004;29:2700–9.
 81. Haynes WM. *CRC Handbook of Chemistry and Physics* 2012–2013. 93rd ed. Boca Raton, FL: CRC Press/Taylor and Francis, 2012.
 82. Vaupel P, Kallinowski F, Okunieff P. Blood flow, oxygen and nutrient supply, and metabolic microenvironment of human tumors: A review. *Cancer Res* 1989;49:6449–65.
 83. Zachos TA, Aiken SW, DiResta GR, Healey JH. Interstitial fluid pressure and blood flow in canine osteosarcoma and other tumors. *Clin Orthop Relat Res* 2001;385:230–6.
 84. Wootton JH, Prakash P, Hsu I-CJ, Diederich CJ. Implant strategies for endocervical and interstitial ultrasound hyperthermia adjunct to HDR brachytherapy for the treatment of cervical cancer. *Phys Med Biol* 2011;56:3967–84.
 85. Buccella C, De Santis V, Feliziani M. Prediction of temperature increase in human eyes due to RF sources. *IEEE Trans Electromagn Compat* 2007;49:825–33.
 86. McFadden ER, Pichurko BM, Bowman HF, Ingenito E, Burns S, Dowling N, et al. Thermal mapping of the airways in humans. *J Appl Physiol* 1985;58:564–70.
 87. Wang J, Fujiwara O. FDTD computation of temperature rise in the human head for portable telephones. *IEEE Trans Microw Theory Techn* 1999;47:1528–34.
 88. Poutanen T, Tikanoja T, Sairanen H, Jokinen E. Normal aortic dimensions and flow in 168 children and young adults. *Clinical physiology and functional imaging* 2003;23:224–9.
 89. Wexler L, Bergel DH, Gabe IT, Makin GS, Mills CJ. Velocity of blood flow in normal human venae cavae. *Circ Res* 1968;23: 349–59.
 90. Azhim A, Katai M, Akutagawa M, Hirao Y, Yoshizaki K, Obara S, et al. Exercise improved age-associated changes in the carotid blood velocity waveforms. *J Biomed Pharm Eng* 2007;1:17–26.
 91. Haemmerich D, Wright AW, Mahvi DM, Lee FT, Webster JG. Hepatic bipolar radiofrequency ablation creates coagulation zones close to blood vessels: A finite element study. *Med Biol Eng Comput* 2003;41:317–23.